

Comprehensive analysis of degradation mechanisms in 18650 Li-Ion cells under prolonged cycling conditions.

Pavel Blažek^{1,3}, Ondřej Klvač^{2,5}, Martin Šedina², Ondřej Čech², Markéta Tkadlecová¹, Zuzana Stravová¹, Tomáš Kazda², Tomáš Zikmund¹, Robert H. Schmitt^{3,4}, Jozef Kaiser¹.

¹Central European Institute of Technology, Brno University of Technology, Brno, Czech Republic

²Department of Electrical and Electronic Technology, Faculty of Electrical Engineering and Communication, Brno University of Technology, Czech Republic

³WZL | RWTH Aachen University, Aachen, Germany

⁴Fraunhofer Institute for Production Technology IPT, Germany

⁵Thermo Fisher Scientific, Vlastimila Pecha 12, Brno, 627 00, Czech Republic

Abstract

Li-ion batteries are a key technology for a wide range of applications including electromobility and stationary energy storage. These applications must operate for several years, and batteries need to meet the demands of these applications over a long period of time. Knowledge of the exact mechanisms of Li-ion battery degradation and their manifestations, as well as insights from the perspective of production quality optimization leading to the extension of the cycle life and safety of these batteries, are thus highly relevant. This study examined the degradation mechanisms in a cylindrical 18650 Li-ion battery over 800 cycles (90% State of Charge, 10% Depth of Discharge) to understand performance fade and structural changes. Periodic micro-CT scans revealed significant geometric alterations in the electrode stack, including delamination and bending towards the cell axis, which correlated with observed capacity loss. Post-mortem analysis using broad ion beam (BIB), scanning electron microscopy (SEM), energy dispersive spectroscopy (EDS), and synchrotron CT confirmed the presence of voids in the cathode active material. Substantial copper deposition was observed exclusively on the anode surface and graphite grains. Elevated levels of phosphorus and fluorine were also detected, likely from electrolyte decomposition and SEI layer formation. These insights shed light on the structural changes and failure modes in cylindrical Li-ion cells during prolonged cycling.

Keywords: Lithium-ion battery degradation, 18650 cylindrical cell, Electrode delamination, Aging

1. Introduction

Lithium-ion batteries (LIBs) have become a key technology for energy storage due to their high energy density, efficiency, and versatility, providing a sufficiently long lifetime. They play a pivotal role in various technologies, from small portable electronic devices to energy

storage systems and electric vehicles [1–3]. One of the most common types of LIB cells is 18650-format, which is a cylindrical cell of 18 mm diameter and 65 mm length. It is used as a standard choice in numerous applications like power tools, electric bicycles and electric cars [4].

Battery aging manifests itself through a multitude of complex symptoms, which reflect changes in micro and macroscopic level. It leads to a decrease in capacity, an increase in internal resistance, and physical changes such as swelling and delamination of electrode layers. It can lead not only to deterioration of performance but also damage battery structure, affect the safety of battery usage, and even culminate in complete battery failure[5–15]. The issue of battery aging is a very broad topic; further described are those processes that have been the subject of research in this paper.

During cycling, the electrodes undergo volumetric changes manifested at the level of whole electrodes as well as individual grains of electroactive material [16–18]. This is mainly due to electrochemical processes involving lithium-ion intercalation and also lattice structural changes [8]. Temperature changes induced by high C-rate also play an essential role [20]. These effects in the cylindrical cells lead to the deformation of the electrodes and their buckling towards the center of the battery. This can result in delamination of the electroactive material and, in extreme cases, disruption of the separator. This phenomenon can be partially counteracted by the use of a central pin - a metal tube that fills the space in the center of the cylindrical cell, which, however, increases the weight [16].

Volume changes are also a cause of particle cracking [15,21,22]. It can lead to the material losing contact with the surrounding matrix, making it inactive and decreasing the capacity. Moreover, during cracking, the existing SEI layer is disrupted and starts to grow on the newly formed surfaces. This consumes lithium ions, resulting in further capacity loss. An additional risk lies in the possibility of lithium dendrite formation manifesting itself mainly at higher loads and lower temperatures [10,23,24].

In the application of very high currents and operation of the cell outside the voltage operating window, dissolution of the current collectors may also occur. The cases of anodic oxidation of the copper collector and deposition of Cu ions on the cathode surface increasing its volume have been described [25]. Also, copper can form an internal short circuit through the formation of Cu dendrites. Rarely has the deposition of copper on the surface of the anode or individual grains been described. The reduction of copper dissolved in the electrolyte by reaction with the SEI layer compounds is assumed [26,27].

Evidently, the processes contributing to battery degradation and aging are complex, and their deeper understanding is crucial for the further development of LIBs. X-ray-based techniques are suitable for their investigation due to their non-destructive character and can also be used for in-situ analysis, where a scan is performed after a certain number of electrochemical cycles. This includes X-ray radiography [28] as well as advanced CT methods [29,30]. It is possible to achieve resolution from micrometers when analyzing whole cells down to sub-micrometer resolution of small pieces of electrode materials and detect even mild structural changes [31,32].

With scanning electron microscopy (SEM), even higher resolution can be achieved to observe individual grains, their cracking, and the growth of the SEI layer [11,33–38]. In combination with electron dispersive spectroscopy (EDS), it is also possible to determine the elemental composition and its changes after electrochemical cycling [39,40].

Since the cell must be disassembled before analysis, it is advisable to discharge it for safety reasons, to avoid short-circuiting during further handling, and to minimize contact with air. Argon gloveboxes are typically used for this purpose. The separated electrodes are then examined from the surface or cross-section. The materials are often brittle and can be damaged by mechanical stress. For this reason, focused ion beam (FIB) also allowing FIB/SEM 3D reconstruction [41–43] or broad ion beam (BIB) [8,44–47] techniques are often used for sample preparation, which sputter the material without mechanical force and allow the samples to be observed in their native state [7,8].

In this study, we detailly examine 18650-type LIB in the fresh state and during 800 cycles of charging and discharging, observing various symptoms of degradation. The analysis of the cycled cell was focused on the structural and chemical changes, their correlation with the micro-CT (X-ray computed tomography) analysis, and comparison with another uncycled cell using SEM/EDS analysis. We applied CT and virtual unrolling techniques to quantify geometrical changes in the whole battery in the fresh state and after every 200 cycles of charging and discharging. With each scan, we also analyze changes in battery capacity and hysteresis together with an impedance analysis by Electrochemical Impedance Spectroscopy (EIS). We also performed further analysis of the cycled battery after 800 cycles and another battery of the same manufacturing batch in a fresh state. To observe pieces of cathodes with higher resolution we used sub-micron CT and sSEM and analyzed elemental composition using EDS.

2. Materials and methods

2.1. Samples

We investigated LIB Samsung INR18650-29E (manufacturer stated capacity 2860 mAh) based $\text{LiNi}_x\text{Mn}_y\text{Co}_{1-x-y}\text{O}_2$ (NMC), the most used cathode materials in LIBs. We used two pieces of accumulators from the same manufacturing batch. The first one, fresh cell, was used for destructive analysis before cycling, and the other one was used for long-term cycling and degradation study. After the cycling was finished, we used it for destructive analysis of the effects of aging.

2.2. Aging and electrical analysis

The test cell was characterized by a baseline test using two cycles in the full manufacturer-defined voltage range of 2.5 - 4.2 V at 0.1C/0.1C, 0.2C/0.2C, 0.2C/0.5C and 0.2C/1C (charge/discharge). EIS was performed at 100% SoC during 0.1/0.1 C cycle in a frequency range from 1 MHz to 30 mHz, with an amplitude of 10 mV, followed by CT scanning. The CCCV method was used with the limiting current set to 0.02 C. The initial test was followed by long-term cycling at 1 C using the CCCV method with a limit current of 0.02 C in the range of 90% SoC and 10% DoD for 200 cycles, followed by a baseline test and subsequently by CT scanning. This process was repeated until 800 cycles were reached. After the last baseline

test and CT analysis, the cell was disassembled and analyzed by SEM. The electrochemical measurements were performed with a Bio-Logic battery cycler BCS-815 with an EIS module.

2.3. Micro CT analysis

The whole LIB was analyzed by micro CT in the fresh state, after 200, 400, 600, and 800 cycles. For these measurements, we used a Thermo Scientific HeliScan microCT system equipped with a flat panel detector with a resolution of 3072x3072 px² and pixel size 139 μ m and 160 kV microfocus tube. The whole battery was analyzed by one scan with a space-filling helical trajectory, which allowed the use of higher geometrical magnification and increased the signal-to-noise ratio while avoiding cone-beam artifacts. The X-ray tube was set to 150 kV, and the beam was filtered with 0.2 mm of stainless steel and 0.5 mm thick Sn foils to reduce beam-hardening. To obtain sufficient signal, the exposure time was set to 0.65 s, and five radiographs were averaged in each of the 5400 projections per scan. The data were reconstructed with the iterative algorithm in software provided by the manufacturer. An algorithm for sample drift correction and the self-calibration algorithm [48] were used to correct for geometrical errors. The reconstructed volume size was approximately 22 x 22 x 73 mm³ with (8 μ m)³ voxel size.

The virtual unrolling technique was applied to all the whole-cell datasets in Thermo Scientific Avizo. We used the procedure described in [49]. The cathode was segmented using the multithresholding method, and morphological operations such as opening/closing were applied. We analyzed the distance from the core on the segmented cathode and compared results between datasets. An unrolled distance map then allows for the assessment of cathode position and deformities in the entire cell volume.

2.4. Sample preparation for SEM, EDS, and submicron CT

Before disassembly, batteries were deeply discharged to 1 V with a current of 0.05 C. Inside the Ar-filled glovebox, the metal case was cut about 1 mm below the edge of the positive pin using a manual tube cutter. The CT inspection revealed that there is a free space inside with minimal risk of electrode damage. The positive pin was then removed using pliers, and the metal case was unrolled to approximately half the cell's height. The electrolyte was dried by leaving the cell under a vacuum in the glovebox antechamber for about one hour. Pieces of the individual electrodes were cut from the unrolled section using scissors. Further manipulation took place outside the glovebox. The cell was cut across on the negative pin side with a hacksaw about 1 cm above the pin edge. The metal case in this area serves as a mechanical fixation and prevents structure shifting during cross-section preparation through the entire structure. This specimen was then mechanically ground by 30, 15, 8, and 5 μ m grain size SiC grinder papers with isopropanol. The Broad Ion Beam (BIB) polisher model 1061 SEM Mill (Fischione Instruments) was used for further sample preparation. The individual electrodes were prepared in cross-section mode, and the whole structure in planar mode using Cryo cooling. SEM imaging and EDS analysis were performed on a Scios 2 scanning electron microscope (Thermo Fischer Scientific).

For nanoCT, pieces of approximately 0.5 x 2 mm were cut from individual electrodes with a razor blade. The samples were inserted into a Kapton tube and fixed with molten ethylene

carbonate. For SEM/CT correlative analysis, the sample was first polished using BIB, then SEM analysis was performed, and finally placed in the Kapton tube.

2.5. Submicron CT

We used the unpolished part of the cell and unrolled the electrodes. A piece of it was cut to dimensions approximately 0.5x2 mm. This piece was then fixed on a special holder. It was inserted in a Kapton tube and poured with ethylene carbonate to reduce oxidation. The sample was then imaged using nanoCT Rigaku nano3DX with Mo target, 50 kV tube voltage, 35 s exposure time, 800 projections, and voxel size of 0.54 μm .

3. Results and discussion

Continuous measurements revealed capacity decrease during cell cycling (Figure 1 a). We also observed that after interrupting the cycling for analysis with CT, regeneration occurred, and capacity was increased. This effect was most significant after 200 and 400 cycles. The most considerable capacity reduction of 20.8 % occurred after the first 200 cycles. After that, the capacity regenerated to 90.8 % of the original value and, during another 200 cycles, decreased by a similar value as in the first 200 cycles. This effect repeated also between 400 and 600 cycles. A notable capacity reduction of 11.3 % occurred between 600 and 800 cycles as well. In total, capacity dropped by 30.5 % after 800 cycles (see Table 1).

Table 1. Capacity and capacity retention in different stages of cycling.

Cycle number	Capacity/mAh	Capacity retention/%
1	2165	-
200	1714	20.8%
400	1668	23.0%
600	1717	20.7%
800	1505	30.5%

The discharge characteristics at different C-rates before and after cycling are shown in Figure 1 b.. At all C-rates after 800 cycles of cycling, there was a decrease in the achieved capacity and, at the same time, a decrease in the discharge plateau. The capacity at 0.1 C load has been reduced from 2865 mAh, which is equivalent to the capacity declared by the manufacturer, to 2442 mAh (14.8 % capacity drop). At 0.2C load, the capacity dropped from 2807 to 2344 mAh (16.5% capacity drop). At loads of 0.5C and 1C, the capacity dropped by 19.2 % and 22.1 %, respectively. It is evident that cycling did not only lead to a decrease in capacity but also to a decrease in load ability at higher C-rates.

The change in capacity during the baseline tests is shown in Tab.2. When comparing the capacities of the characterization cycles, a significant change can be seen after 200 and 800 cycles, where after 200 cycles, there was a significant change in capacity but stability at higher loads was maintained. Thus, at a load of 1C, there was a 4.2 % decrease before cycling and a 4.5 % decrease after cycling compared to a current of 0.1C. Another significant change in this parameter occurred after 800 cycles.

The hysteresis changes at different C-rates during cycling, as shown in Figure 1 c. It is evident that the hysteresis increases with increasing C-rate and is highest at 1 C. After 200 cycles, there was an increase in hysteresis at all C-rates. Its value then remained stable

during the following cycling until the last 200 cycles, when the value increased again significantly for all C-rates. This increase of hysteresis is in correlation with the significant capacity drop during the last 200 cycles of cycling and corresponds to the large capacity drop at a current load of 1 C that was observed at the end of cycling.

The EIS analysis revealed that the charge transfer resistance (R_{ct}) at the beginning of cycling was double that after 200 cycles, which is visible in Nyquist plots in Figure 1 d. This is due to the changes in the structure at the beginning of cycling, which lead to improved contact with the electrolyte. Liu et al. give a similar description of this change [50]. Subsequently, R_{ct} increases with cycling, and after 800 cycles, its value approaches the original values before cycling.

The dV/dQ analysis before cycling and after a different number of cycles (200, 400, 600, and 800) is visualized in Figure 2. The figure shows the activity of the contained materials at the anode and at the cathode and their gradual degradation. An anodic peak at 3.42 V and cathodic at 3.38 V is related to lithiation of graphite anode [51]. After 200 cycles, both peaks shifted to a higher voltage, and peaks were less evident. During the cycling, peaks become more evident and, at the same time, change position close to 3.5 V. The magnitude of the anode-related peak after 200, 400, and 600 cycles was similar; however, after 800 cycles, the peak magnitude decreased, indicating a decrease in the activity of the anode material. This drop might be associated with a higher drop in capacity at a high C-rate after 800 cycles. Another very significant anodic peak can be observed at a potential of about 3.65 V. This peak is related to the transition from a hexagonal to a monoclinic lattice of the NMC532 cathode [52]. Its activity gradually decreases, with the most significant change can be observed after the first 200 cycles and then after the last 200 cycles of cycling. The anodic peak around 4.1 V is then associated with high Ni cathode materials such as NMC811 or NCA (10.1149/2.0021707jes) and represents the H2 to H3 phase transition. The small anodic peak located around 3.8 V represents the transition from the M to the H2 phase. The peak around 4.1 V was relatively stable for the first 400 cycles, but it dropped significantly after 600 and 800 cycles. This decrease may then be related to the capacity drop during the subsequent cycling, when the partial regeneration of the battery capacity no longer occurred when cycling started again.

Table 2. Degradation under different loads during long-term cycling.

Cycle number	Capacity/mAh				Capacity drop/%		
	0.1C	0.2C	0.5C	1C	0.2C vs 0.1C	0.5C vs 0.1C	1C vs 0.1C
0	2865	2807	2742	2744	98.0%	95.7%	95.8%
200	2660	2591	2591	2541	97.4%	97.4%	95.5%
400	2583	2555	2503	2490	98.9%	96.9%	96.4%
600	2478	2459	2400	2363	99.2%	96.9%	95.4%
800	2442	2344	2215	2139	96.0%	90.7%	87.6%

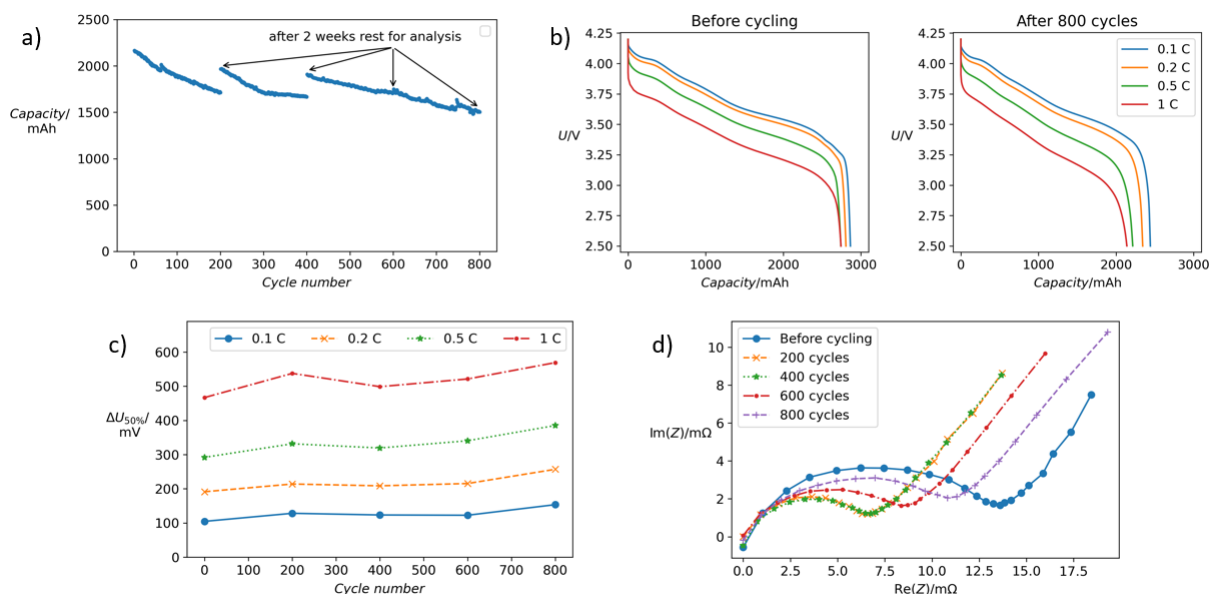


Figure 1. a) Capacity decreases due to cycling, b) Discharging profiles at different C-rate before and after cycling, c) Changes of hysteresis at different c-rates during cycling, d) EIS analysis in different stages of long-term cycling.

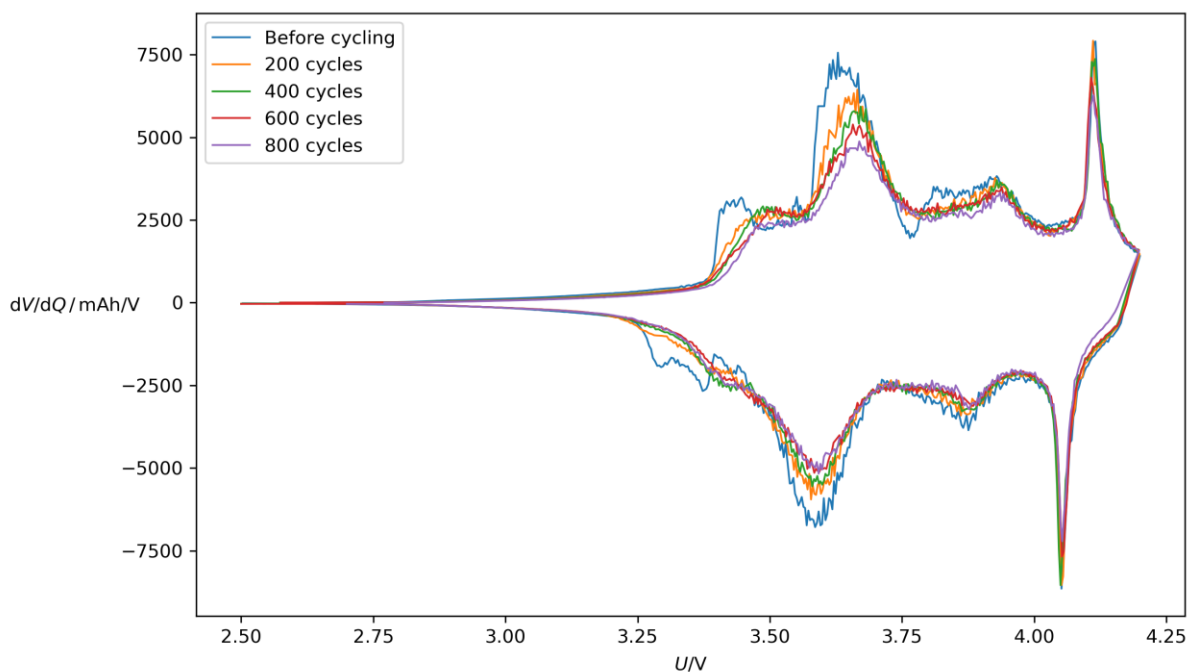


Figure 2. dQ/dV analysis for INR18650-29E cell before cycling and after 200, 400, 600 and 800 cycles.

Prolonged cycling of the cell caused damage to the inner geometry of the cell. The electrodes are deformed, and the electroactive material is cracked and delaminated from the current collector. These deformations are clearly visible in tomographic cross-sections (Figure 3) as well as an SEM image of the cross-section through the whole structure (Figure 4). The deformation is first visible after 200 cycles on the first three windings of the electrode stack and is getting more pronounced with cycling. After 800 cycles, they reach up to the seventh winding of electrodes. SEM image (Figure 4) shows, in addition to electrode waving, cracks, and loss of contact with the current collector, also loss of contact of the anode with the separator and, therefore, with the opposite cathode.

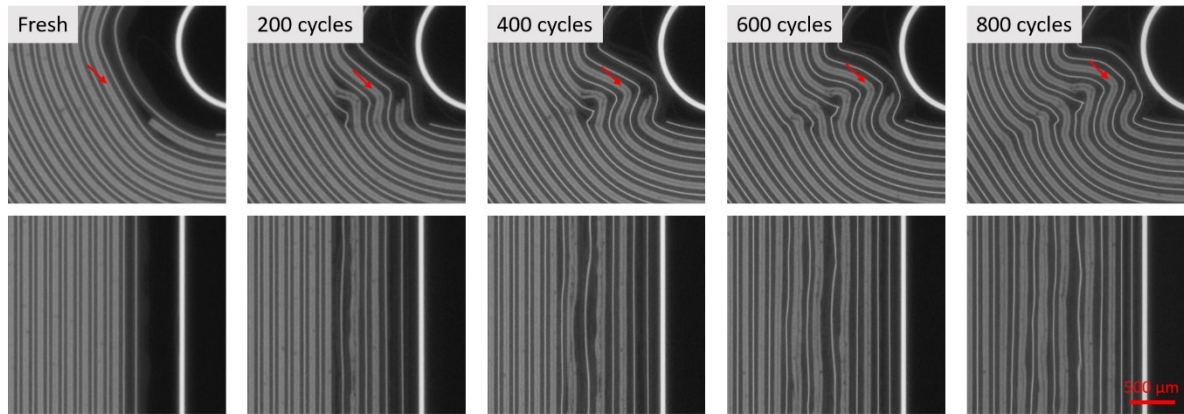


Figure 3. Tomographic cross-sections, detail of the deformation's development through cycling. Top row: Axial view, bottom row: axial view. Red arrow point to the highest deformation present in the innermost winding, which is the same position as show in Figure 5.

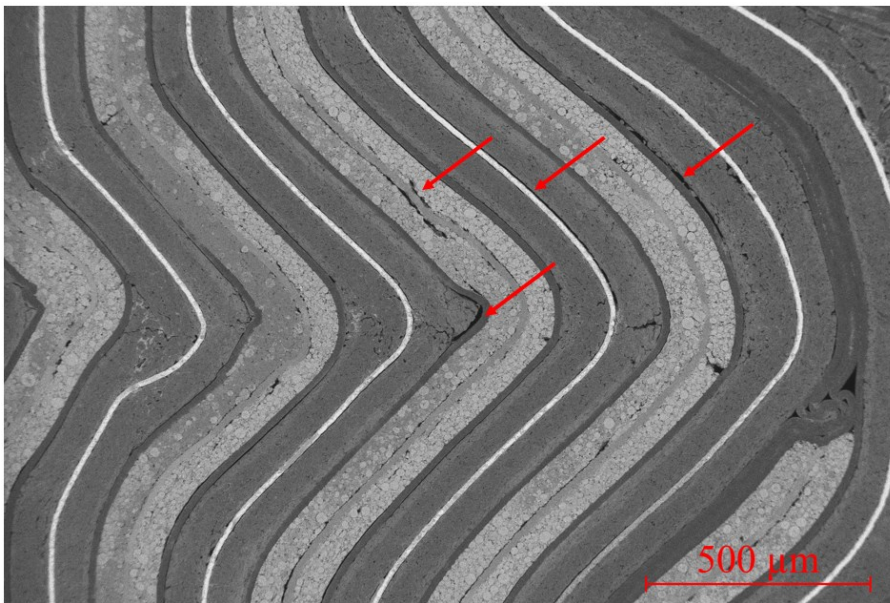


Figure 4. Detail of cross-section through the whole battery structure. Electrodes are bending towards the central pin, arrows points to loss of contact with separator and current collector.

The virtual unrolling technique allowed us to visualize the geometry of the cathode across the entire volume at different cycling stages. Electrode deformations appear as vertical stripes in the distance-from-core map. Stripes visible in the fresh dataset (Figure 5 a) that persist in data from the cycled cell indicate that the electrode deviates from an ideal spiral. Deformities arising in the inner winding due to cycling are also evident in the unrolled data as additional stripes in the corresponding sections. These deformities extend through the entire height of the electrode spiral and become more pronounced with an increasing number of cycles. A limitation of this unrolled map is the presence of artifacts in the form of sharp borders between horizontal sections. These artifacts stem from the unrolling algorithm in Avizo, which required dividing the data into sections to reduce computational demands and introduced interpolation errors that likely struggled to handle deviations from the ideal spiral. Due to these artifacts, this data cannot be used for quantitative measurements, such as comparing distance from the core between datasets. However, the unrolled data show a cathode length increase of 3.5 mm (0.5%) over 800 cycles (see Figure

6), likely resulting from increased bending and deformations. The data shows that the most prominent change occurred again after the first 200 cycles and after the last 200 cycles, which correlates with the results of electrochemical measurements. The change of hysteresis occurred at a similar time; at the last 200 cycles, there was a significant decrease in capacity at high C-rates.

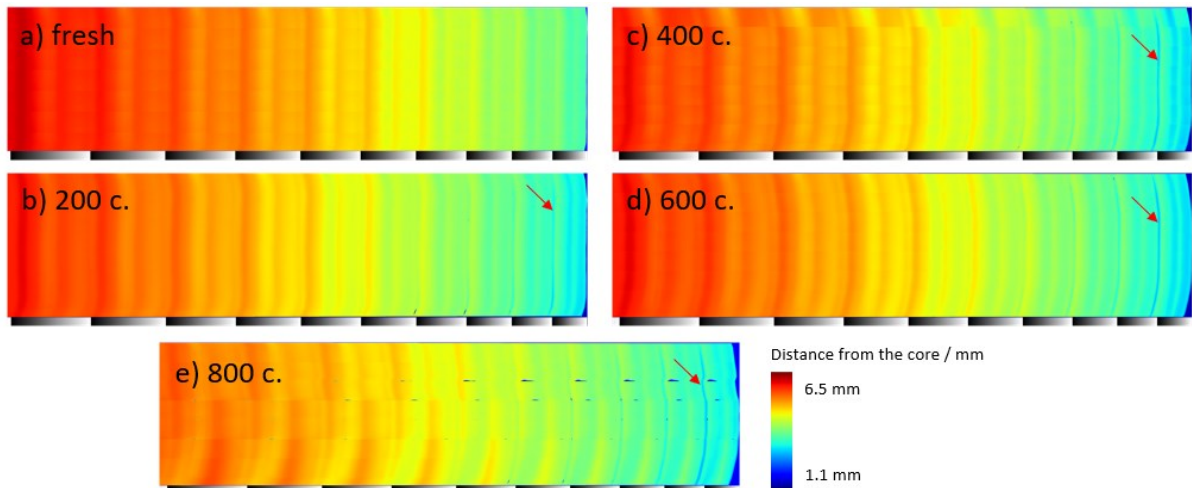


Figure 5. Visualization of 10 innermost windings of the unrolled cathode as an unrolled distance from the cell core color map. Red arrows point to the highest deformation present in the innermost winding, which is the same position as shown in Figure 3.

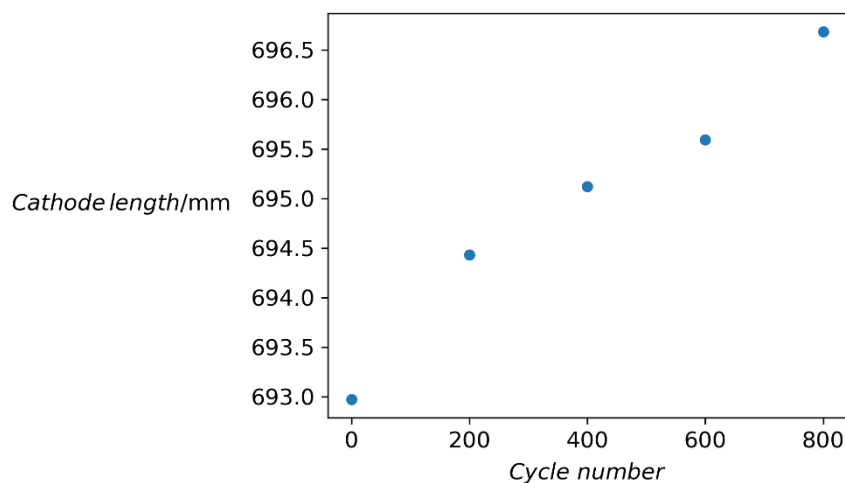


Figure 6. Length of cathode after unrolling

Cross-section images of the fresh cells obtained both by CT (Figure 3) and SEM (Figure 4) show the manufacturing defects in the structure. These are unfilled areas within the electroactive layer structure and bends of the current collector. These areas correspond to the 'voids' in the CT model. The cause is probably due to the inhomogeneous composition of the cathode paste, where a bubble forms on one side of the current collector. Subsequent pressing leads to its denting and damage of the cathode material particles. Details of these areas are visible in SEM images shown in Figure 7. Analysis of three pieces of the cathode by synchrotron CT (see Supplemental Material A.1) shows the presence of approximately 9 defects / mm² of the cathode with a diameter of $(72 \pm 19) \mu\text{m}$ and volume (26000 ± 19000)

μm^3 . There is a high variance in defects shape and size, but no dependency on the position in the battery or influence due to cycling was discovered.

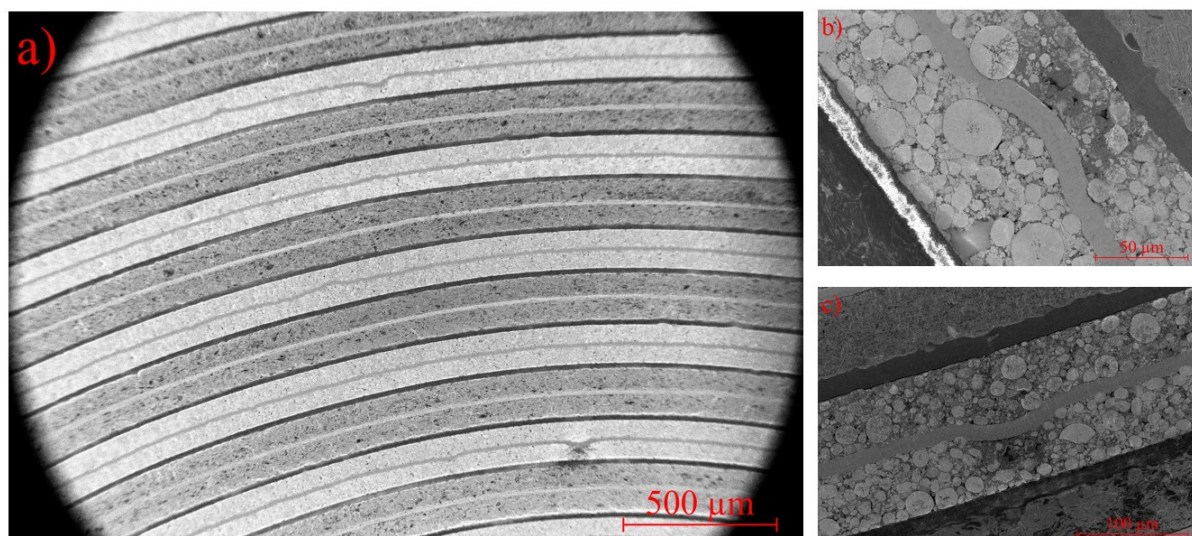


Figure 7. Cross-section SEM image of fresh battery a) Overview of the cross-section b, c) details of the manufacturing defects.

EDS elemental analysis of fresh cell cathode prepared individually revealed that the electroactive material comprises two types of materials with different elemental abundances. As can be seen in the EDS analysis results shown in Table 3 and Figure 8 below one of the cathode materials is NMC532 ($\text{LiNi}_{0.5}\text{Mn}_{0.3}\text{Co}_{0.2}\text{O}_2$) and the other cathode material is most likely NCA ($\text{LiNi}_{0.88}\text{Co}_{0.1}\text{Al}_{0.02}\text{O}_2$). This is consistent with the findings from electrochemical testing of the battery, where a peak associated with the NCA cathode was observed at dQ/dV spectra. The closer analysis showed the local presence of barium sulfate at some grain edges. Also, pieces of aluminum are present between grains. These areas have also increased amounts of sulfur and reach about 2 %.

Table 3 Elemental composition of regions 1-4, as shown in Figure 8 a).

Element	Atomic %			
	Region 1	Region 2	Region 3	Region 4
C	2.9	1.7	1.6	5.7
O	59.1	59.1	56.0	55.6
Mn	0.7	11.2	13.0	0.2
Co	3.0	7.6	7.5	3.2
Ni	33.2	20.1	21.4	34.3
Al	0.9	0.3	0.4	0.8
P	0.2	0.0	0.1	0.2

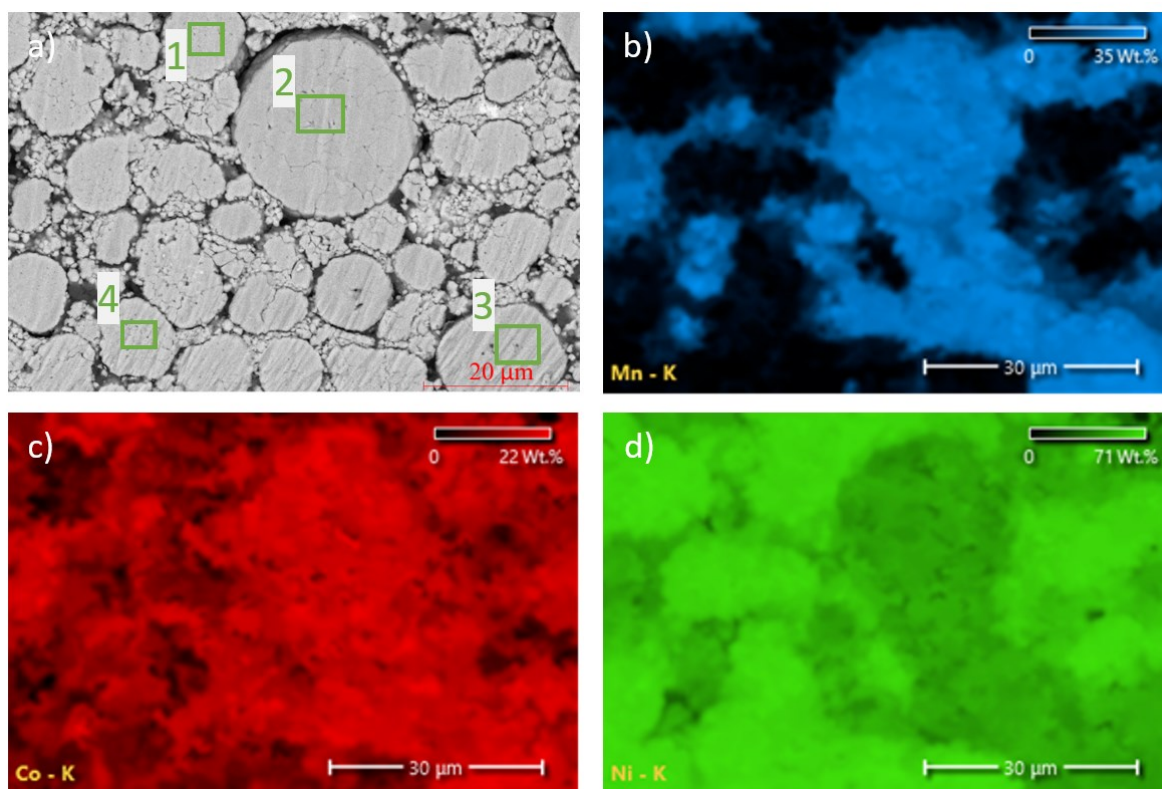


Figure 8. Results of EDS analysis of fresh cathode a) Regions of analysis, the elemental composition of each region is shown in Table 3. Figures show the weight percentage of elements from emission line Kb) Mn c) Co d) Ni

Piece of cathode after 800 cycles was analyzed with microCT and SEM. Same region at the surface of the cathode piece is visualized from both techniques in Figure 9. The analysis of cross-section by EDS showed a 3 % decrease in Ni, a 2 % decrease in Mn, a 1 % decrease in Co for NMC grains, and a 4 % decrease in Ni in NCA grains (Table 4). On the other hand, the oxygen fraction increased by approximately the same amount. Thus, it is probably not a dissolution of transition metal oxides. It can be confirmed by the fact that they were not present on the anode. The particles appear to be more cracked and fragmented after cycling, especially the NMC particles, compared with fresh cell (Figure 10).

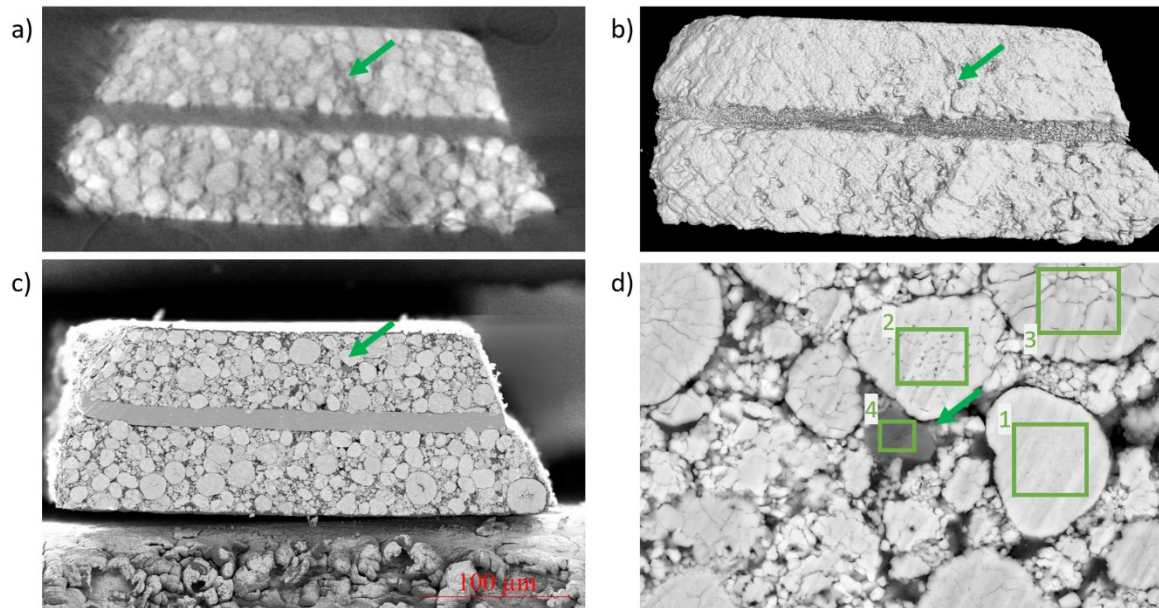


Figure 9. Analysis of a piece of cathode after 800 cycles. a) cross-section from submicron CT, b) 3D render of the CT, c) Image of cathode section on from SEM, d) Detail of SEM image (position shown by green arrows) with elemental composition from EDS.

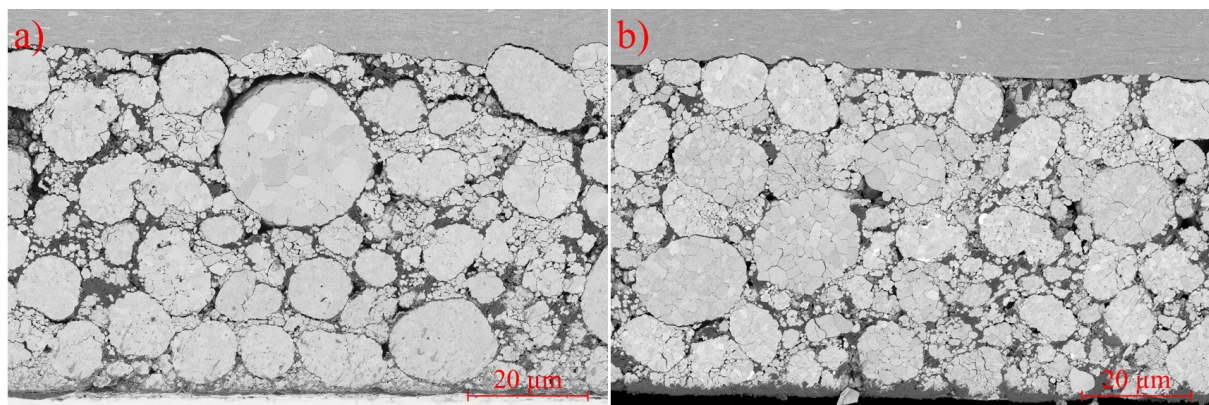


Figure 10. SEM images of cathode cross-section; fresh cell (a); cycled cell (b).

Table 4. Elemental composition of regions (shown in Figure 9 d).

Element	Atomic %			
	Region 1	Region 2	Region 3	Region 4
C	2.6	2.6	2.2	8.6
O	63.2	62.9	64.2	64.7
Al	0.6	0.5	0.3	19.7
Mn	0.6	0.6	10.1	1.3
Co	3.1	3.2	6.6	0.9
Ni	30	30.2	16.6	2.9
S	0	0	0	1.9

In the anode case, a typical layered structure of graphite grains was observed. The analysis also showed minor amounts of fluorine and phosphorus present at the edges of the grains and in the space between them. The origin may be a binder, lithium salt, or a formed SEI layer. The comparison of the anode of the fresh cell and the cycled cell (Figure 11) shows that the gaps between the graphene layers are more expanded in the cycled cell. At the same time, there are pieces of copper between the grains. Copper is also found in a larger amount on the surface of individual grains as part of the SEI layer (Figure 11Figure 12).

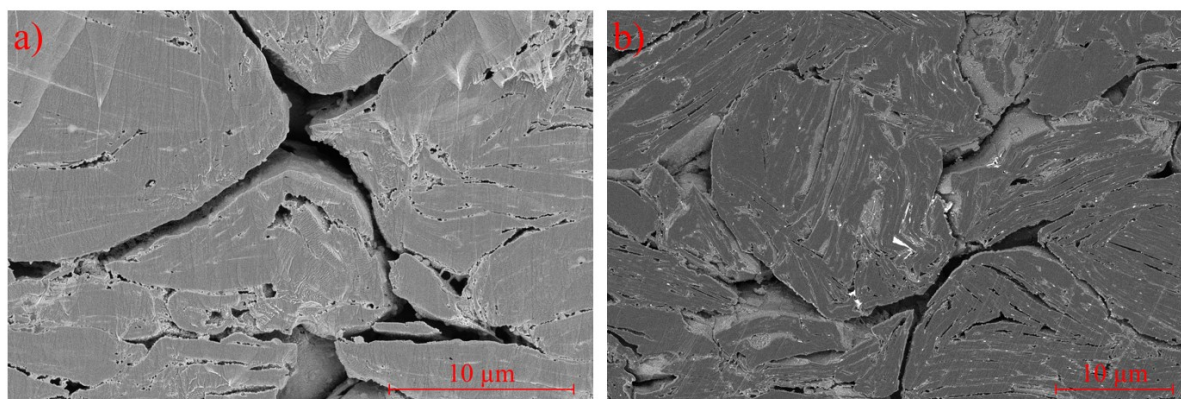


Figure 11. SEM images of anode cross-section; fresh cell (a); cycled cell (b).

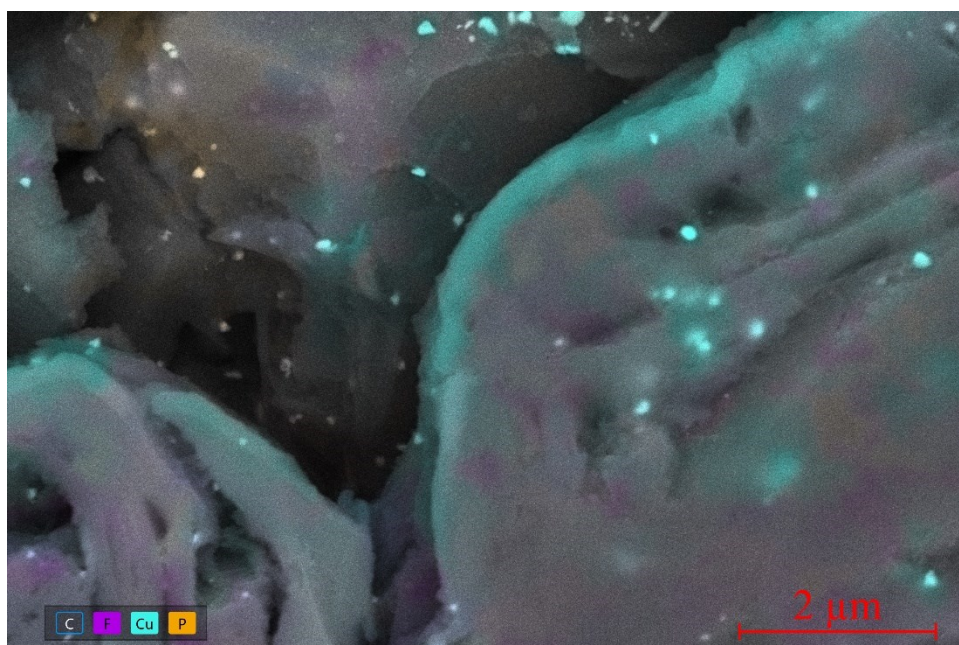


Figure 12. EDS mapping of cycled anode cross-section.

Higher concentrations of copper were additionally detected in a cross-section through the entire cell structure on the surface of the anode as a light stripe (Figure 13). This was confirmed by EDS analysis showing a decreasing copper concentration from the surface toward the center of the anode (Figure 14). The surface of the anode of a fresh cell analyzed in the same way does not show an increased copper concentration.

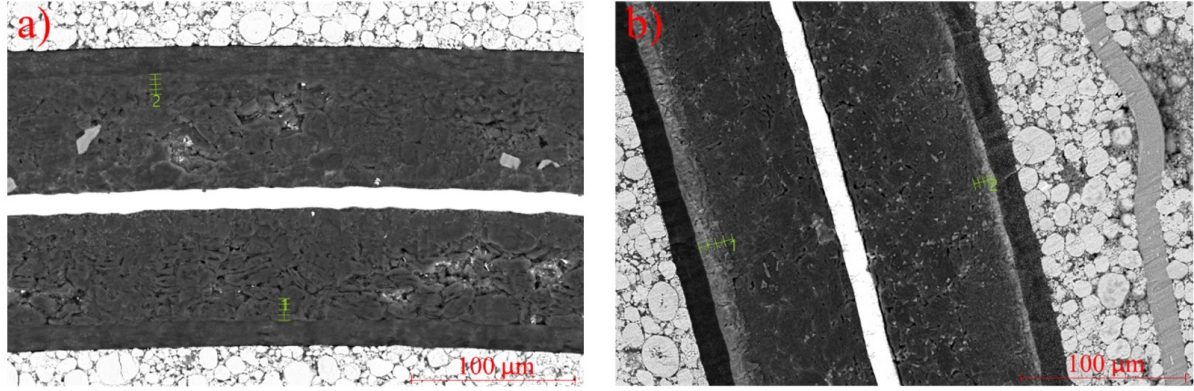


Figure 13. SEM images of whole structure cross-section, study of increased amounts of copper on the anode surface; fresh cell (a); cycled cell (b).

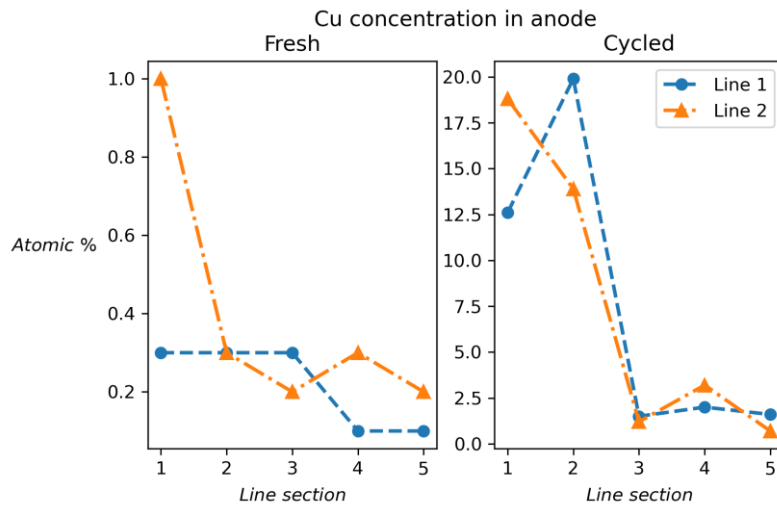


Figure 14. The concentration of Cu on line profiles marked in Figure 13. Detailed results of elemental analysis are in Supplemental material A.2.

4. Conclusions

In this work, we conducted an in-depth analysis of degradation mechanisms in the Samsung 18650 cylindrical cell. The progression observed during cycling aligns with the cell's datasheet specifications. The capacity decrease remains within the expected range and corresponds to EIS measurements. CT analysis revealed mechanical degradation in the electrode material, including delamination and bending toward the cell axis, despite the presence of a metal central pin. This deformation may exert pressure on the polymer separator, increasing the risk of tearing. Delamination and deformation were observed in the inner windings of the electrode spiral in the CT data, both in cross-sections and the unrolled cathode map. As the cycle count increases, these deformations become more pronounced, extending up to the eight innermost windings after 800 cycles. Based on these findings, manufacturers can focus on improving mechanical robustness, for example, by selecting a central pin with a larger diameter.

Analysis revealed voids within the cathode' structure. Cross-sectioning and subsequent BIB/SEM/EDS analysis suggest that NMC grains may experience increased cracking around these void areas. Although no aging-related effects were observed, understanding these defects allows manufacturers to refine the cathode deposition process, such as optimizing

the slurry mixture and improving the coating uniformity, to reduce the incidence of voids and non-uniform layers.

The primary changes identified include the expansion of graphite grains and fracturing of NMC grains around defects. In the cycled material, we observed elevated concentrations of phosphorus (P) and fluorine (F), as well as copper (Cu) concentrations reaching up to 20% on the anode surface and graphite grains. While the P and F concentrations are consistent with typical electrolyte decomposition and SEI layer formation, the source of Cu deposition remains unclear. By analyzing uncycled cells, we ruled out sample preparation as a cause, suggesting that the deposition may result from cycling processes. Literature [26,27] suggests this could involve interactions between Cu ions and SEI layer components, though further investigation is needed for confirmation. Different electrode composition and optimized cycling protocols may prevent these issues.

The extension of the current collector during cycling, which is caused by the pressure of the volumetric changes of active material, leads to deformation of the electrodes, cracking active layers and its delamination from the current collector, which leads to an increase of hysteresis and at the same time to a decrease of capacity due to the loss of contact of the individual particles. The loss of contact of some parts of the electrodes with the separator is then likely to lead to a reduction of stability at higher C-rates. Again, these phenomena can be prevented by a different cell design and cycling protocol. The study provides a detailed understanding of how capacity, resistance, and structural integrity change with long-term cycling. Based on this, manufacturers can develop predictive models for battery life cycle management, allowing better prediction of the aforementioned defects and also estimating when to replace old cells.

5. Acknowledgments

We acknowledge CzechNanoLab Research Infrastructure supported by MEYS CR (LM2023051). We acknowledge Elettra Sincrotrone Trieste for providing access to its synchrotron radiation facilities and for financial support under the IUS internal project, and we thank Lucia Mancini for assistance in using beamline SYRMEP. This work was supported by the project The Energy Conversion and Storage funded as project No CZ 02.01.01/00/22_008/0004617 by Programme Johannes Amos Comenius call Excellent Research. This work was developed in cooperation with Thermo Fisher Scientific Brno.

6. References

- [1] B. Scrosati, J. Garche, Lithium batteries: Status, prospects and future, *Journal of Power Sources* 195 (2010) 2419–2430. <https://doi.org/10.1016/j.jpowsour.2009.11.048>.
- [2] R. Schmich, R. Wagner, G. Hörpel, T. Placke, M. Winter, Performance and cost of materials for lithium-based rechargeable automotive batteries, *Nat Energy* 3 (2018) 267–278. <https://doi.org/10.1038/s41560-018-0107-2>.
- [3] D. Deng, Li-ion batteries: Basics, progress, and challenges, 3 (2015) 385–418.

- [4] V. Muenzel, A.F. Hollenkamp, A.I. Bhatt, J. de Hoog, M. Brazil, D.A. Thomas, I. Mareels, A Comparative Testing Study of Commercial 18650-Format Lithium-Ion Battery Cells, *J. Electrochem. Soc.* 162 (2015) A1592. <https://doi.org/10.1149/2.0721508jes>.
- [5] M. Pin, J. Choi, J.H. Chang, A.S. Schenk, J. Han, S. Wacławek, Y. Kim, J.Y. Cheong, *In situ* X-ray based analysis of anode materials for lithium-ion batteries: Current status and future implications, *Energy Storage Materials* 73 (2024) 103798. <https://doi.org/10.1016/j.ensm.2024.103798>.
- [6] L. Willenberg, P. Dechent, G. Fuchs, M. Teuber, M. Eckert, M. Graff, N. Kürten, D.U. Sauer, E. Figgemeier, The Development of Jelly Roll Deformation in 18650 Lithium-Ion Batteries at Low State of Charge, *Journal of The Electrochemical Society* 167 (2020) 120502. <https://doi.org/10.1149/1945-7111/aba96d>.
- [7] T. Waldmann, A. Iturrondobeitia, M. Kasper, N. Ghanbari, F. Aguesse, E. Bekaert, L. Daniel, S. Genies, I.J. Gordon, M.W. Löble, E.D. Vito, M. Wohlfahrt-Mehrens, Review—Post-Mortem Analysis of Aged Lithium-Ion Batteries: Disassembly Methodology and Physico-Chemical Analysis Techniques, *J. Electrochem. Soc.* 163 (2016) A2149. <https://doi.org/10.1149/2.1211609jes>.
- [8] Kovachev, Schröttner, Gstrein, Aiello, Hanzu, Wilkening, Foitzik, Wellm, Sinz, Ellersdorfer, Analytical Dissection of an Automotive Li-Ion Pouch Cell, *Batteries* 5 (2019) 67. <https://doi.org/10.3390/batteries5040067>.
- [9] S.J. An, J. Li, C. Daniel, D. Mohanty, S. Nagpure, D.L. Wood, The state of understanding of the lithium-ion-battery graphite solid electrolyte interphase (SEI) and its relationship to formation cycling, *Carbon* 105 (2016) 52–76. <https://doi.org/10.1016/j.carbon.2016.04.008>.
- [10] T. Waldmann, M. Wilka, M. Kasper, M. Fleischhammer, M. Wohlfahrt-Mehrens, Temperature dependent ageing mechanisms in Lithium-ion batteries – A Post-Mortem study, *Journal of Power Sources* 262 (2014) 129–135. <https://doi.org/10.1016/j.jpowsour.2014.03.112>.
- [11] J. Cheng, X. Li, Z. Wang, H. Guo, Mechanism for capacity fading of 18650 cylindrical lithium ion batteries, *Transactions of Nonferrous Metals Society of China* 27 (2017) 1602–1607. [https://doi.org/10.1016/S1003-6326\(17\)60182-1](https://doi.org/10.1016/S1003-6326(17)60182-1).
- [12] M. Ecker, N. Nieto, S. Käbitz, J. Schmalstieg, H. Blanke, A. Warnecke, D.U. Sauer, Calendar and cycle life study of Li(NiMnCo)O₂-based 18650 lithium-ion batteries, *Journal of Power Sources* 248 (2014) 839–851. <https://doi.org/10.1016/j.jpowsour.2013.09.143>.
- [13] K. Dai, Z. Wang, G. Ai, H. Zhao, W. Yuan, X. Song, V. Battaglia, C. Sun, K. Wu, G. Liu, The transformation of graphite electrode materials in lithium-ion batteries after cycling, *Journal of Power Sources* 298 (2015) 349–354. <https://doi.org/10.1016/j.jpowsour.2015.08.055>.
- [14] G. Kwak, J. Park, J. Lee, S. Kim, I. Jung, Effects of anode active materials to the storage-capacity fading on commercial lithium-ion batteries, *Journal of Power Sources* 174 (2007) 484–492. <https://doi.org/10.1016/j.jpowsour.2007.06.169>.
- [15] H.-J. Kim, T. Krishna, K. Zeb, V. Rajangam, C.V.V.M. Gopi, S. Sambasivam, K.V.G. Raghavendra, I.M. Obaidat, A Comprehensive Review of Li-Ion Battery Materials and Their Recycling Techniques, *Electronics* 9 (2020) 1161. <https://doi.org/10.3390/electronics9071161>.
- [16] T. Waldmann, S. Gorse, T. Samtleben, G. Schneider, V. Knoblauch, M. Wohlfahrt-Mehrens, A Mechanical Aging Mechanism in Lithium-Ion Batteries, *Journal of The Electrochemical Society* 161 (2014) A1742–A1747. <https://doi.org/10.1149/2.1001410jes>.

- [17] J.H. Lee, H.M. Lee, S. Ahn, Battery dimensional changes occurring during charge/discharge cycles—thin rectangular lithium ion and polymer cells, *Journal of Power Sources* 119–121 (2003) 833–837. [https://doi.org/10.1016/S0378-7753\(03\)00281-7](https://doi.org/10.1016/S0378-7753(03)00281-7).
- [18] M. Ko, S. Chae, J. Cho, Challenges in Accommodating Volume Change of Si Anodes for Li-Ion Batteries, *ChemElectroChem* 2 (2015) 1645–1651. <https://doi.org/10.1002/celc.201500254>.
- [19] N. Zhang, H. Tang, Dissecting anode swelling in commercial lithium-ion batteries, *Journal of Power Sources* 218 (2012) 52–55. <https://doi.org/10.1016/j.jpowsour.2012.06.071>.
- [20] S. Yun, C. Kim, Influences of thermal volume changes in LiMn₂O₄ particles on the performance of a Li-ion battery, *J Mech Sci Technol* 32 (2018) 3233–3239. <https://doi.org/10.1007/s12206-018-0625-7>.
- [21] C. Lin, A. Tang, H. Mu, W. Wang, C. Wang, Aging Mechanisms of Electrode Materials in Lithium-Ion Batteries for Electric Vehicles, *Journal of Chemistry* 2015 (2015) 1–11. <https://doi.org/10.1155/2015/104673>.
- [22] A.M. Boyce, E. Martínez-Pañeda, A. Wade, Y.S. Zhang, J.J. Bailey, T.M.M. Heenan, D.J.L. Brett, P.R. Shearing, Cracking predictions of lithium-ion battery electrodes by X-ray computed tomography and modelling, *Journal of Power Sources* 526 (2022) 231119. <https://doi.org/10.1016/j.jpowsour.2022.231119>.
- [23] M. Broussely, Ph. Biensan, F. Bonhomme, Ph. Blanchard, S. Herreyre, K. Nechev, R.J. Staniewicz, Main aging mechanisms in Li ion batteries, *Journal of Power Sources* 146 (2005) 90–96. <https://doi.org/10.1016/j.jpowsour.2005.03.172>.
- [24] Q. Liu, C. Du, B. Shen, P. Zuo, X. Cheng, Y. Ma, G. Yin, Y. Gao, Understanding undesirable anode lithium plating issues in lithium-ion batteries, *RSC Adv.* 6 (2016) 88683–88700. <https://doi.org/10.1039/C6RA19482F>.
- [25] R. Guo, L. Lu, M. Ouyang, X. Feng, Mechanism of the entire overdischarge process and overdischarge-induced internal short circuit in lithium-ion batteries, *Sci Rep* 6 (2016) 30248. <https://doi.org/10.1038/srep30248>.
- [26] T. Langner, T. Sieber, J. Acker, Studies on the deposition of copper in lithium-ion batteries during the deep discharge process, *Sci Rep* 11 (2021) 6316. <https://doi.org/10.1038/s41598-021-85575-x>.
- [27] M. Flügel, T. Waldmann, M. Kasper, M. Wohlfahrt-Mehrens, Detection of Copper Deposition on Anodes of Over-Discharged Lithium Ion Cells by GD-OES Depth Profiling, *ChemPhysChem* 21 (2020) 2047–2050. <https://doi.org/10.1002/cphc.202000333>.
- [28] A. Schilling, P. Gumbel, M. Möller, F. Kalkan, F. Dietrich, K. Dröder, X-ray Based Visualization of the Electrolyte Filling Process of Lithium Ion Batteries, *J. Electrochem. Soc.* 166 (2019) A5163–A5167. <https://doi.org/10.1149/2.0251903jes>.
- [29] R.F. Ziesche, T. Arlt, D.P. Finegan, T.M.M. Heenan, A. Tengattini, D. Baum, N. Kardjilov, H. Markötter, I. Manke, W. Kockelmann, D.J.L. Brett, P.R. Shearing, 4D imaging of lithium-batteries using correlative neutron and X-ray tomography with a virtual unrolling technique, *Nature Communications* 11 (2020) 1–11. <https://doi.org/10.1038/s41467-019-13943-3>.

- [30] M. Kodama, S. Komiyama, A. Ohashi, N. Horikawa, K. Kawamura, S. Hirai, High-pressure in situ X-ray computed tomography and numerical simulation of sulfide solid electrolyte, *Journal of Power Sources* 462 (2020) 228160. <https://doi.org/10.1016/j.jpowsour.2020.228160>.
- [31] P. Blazek, P. Westenberger, S. Erker, A. Brinek, T. Zikmund, D. Rettenwander, N. Peter, J. Keckes, J. Kaiser, T. Kazda, P. Vyrubal, M. Macak, J. Todt, Axially and radially inhomogeneous swelling in commercial 18650 Li-ion battery cells, *Journal of Energy Storage* 52 (2022) 104563. <https://doi.org/10.1016/j.est.2022.104563>.
- [32] P. Pietsch, V. Wood, X-Ray Tomography for Lithium Ion Battery Research: A Practical Guide, *Annual Review of Materials Research* 47 (2017) 451–479. <https://doi.org/10.1146/annurev-matsci-070616-123957>.
- [33] Y. Li, J. Guo, K. Pedersen, L. Gurevich, D.-I. Stroe, Recent Health Diagnosis Methods for Lithium-Ion Batteries, *Batteries* 8 (2022) 72. <https://doi.org/10.3390/batteries8070072>.
- [34] N. Williard, B. Sood, M. Osterman, M. Pecht, Disassembly methodology for conducting failure analysis on lithium-ion batteries, *Journal of Materials Science: Materials in Electronics* 22 (2011) 1616–1630. <https://doi.org/10.1007/s10854-011-0452-4>.
- [35] C. Kang, Y.W. Cho, Imaging of electric failure in Si-alloy/graphite-blended anodes for Li-ion batteries, *Journal of Power Sources* 485 (2021) 229311. <https://doi.org/10.1016/j.jpowsour.2020.229311>.
- [36] H.S. Kang, P. Santhoshkumar, J.W. Park, G.S. Sim, M. Nanthagopal, C.W. Lee, Glass ceramic coating on $\text{LiNi}_0.8\text{Co}_0.1\text{Mn}_0.1\text{O}_2$ cathode for Li-ion batteries, *Korean J. Chem. Eng.* 37 (2020) 1331–1339. <https://doi.org/10.1007/s11814-020-0570-x>.
- [37] Y. Shi, X. Pan, B. Li, M. Zhao, H. Pang, Co_3O_4 and its composites for high-performance Li-ion batteries, *Chemical Engineering Journal* 343 (2018) 427–446. <https://doi.org/10.1016/j.cej.2018.03.024>.
- [38] D.J. Miller, C. Proff, J.G. Wen, D.P. Abraham, J. Bareño, Observation of Microstructural Evolution in Li Battery Cathode Oxide Particles by In Situ Electron Microscopy, *Advanced Energy Materials* 3 (2013) 1098–1103. <https://doi.org/10.1002/aenm.201300015>.
- [39] U. Golla-Schindler, L. Han, P. Gnauck, F. Khanom, T. Bernthaler, G. Schneider, Microstructural and Analytic Characterisation of Li-Ion Batteries by Correlative EDS, SIMS, Light-, Raman-, Ion- and Electron Microscopy, *Microscopy and Microanalysis* 25 (2019) 1756–1757. <https://doi.org/10.1017/S1431927619009516>.
- [40] W. Qi, L. Ben, H. Yu, W. Zhao, G. Zhao, X. Huang, Improving the rate capability of a SiO_x /graphite anode by adding LiNO_3 , *Progress in Natural Science: Materials International* 30 (2020) 321–327. <https://doi.org/10.1016/j.pnsc.2020.05.008>.
- [41] H. Liu, J.M. Foster, A. Gully, S. Krachkovskiy, M. Jiang, Y. Wu, X. Yang, B. Protas, G.R. Goward, G.A. Botton, Three-dimensional investigation of cycling-induced microstructural changes in lithium-ion battery cathodes using focused ion beam/scanning electron microscopy, *Journal of Power Sources* 306 (2016) 300–308. <https://doi.org/10.1016/j.jpowsour.2015.11.108>.
- [42] M. Ender, J. Joos, T. Carraro, E. Ivers-Tiffée, Three-dimensional reconstruction of a composite cathode for lithium-ion cells, *Electrochemistry Communications* 13 (2011) 166–168. <https://doi.org/10.1016/j.elecom.2010.12.004>.

- [43] Y.K. Chen-Wiegart, R. DeMike, C. Erdonmez, K. Thornton, S.A. Barnett, J. Wang, Tortuosity characterization of 3D microstructure at nano-scale for energy storage and conversion materials, *Journal of Power Sources* 249 (2014) 349–356. <https://doi.org/10.1016/j.jpowsour.2013.10.026>.
- [44] M. Indrikova, S. Grunwald, F. Golks, A. Netz, B. Westphal, A. Kwade, The Morphology of Battery Electrodes with the Focus of the Conductive Additives Paths, *J. Electrochem. Soc.* 162 (2015) A2021. <https://doi.org/10.1149/2.0441510jes>.
- [45] A. Sakuda, A. Hayashi, M. Tatsumisago, Sulfide Solid Electrolyte with Favorable Mechanical Property for All-Solid-State Lithium Battery, *Sci Rep* 3 (2013) 2261. <https://doi.org/10.1038/srep02261>.
- [46] T. Cheng, Z. Ma, R. Gu, R. Chen, Y. Lyu, A. Nie, B. Guo, Cracks Formation in Lithium-Rich Cathode Materials for Lithium-Ion Batteries during the Electrochemical Process, *Energies* 11 (2018) 2712. <https://doi.org/10.3390/en11102712>.
- [47] T.R. Tanim, E.J. Dufek, M. Evans, C. Dickerson, A.N. Jansen, B.J. Polzin, A.R. Dunlop, S.E. Trask, R. Jackman, I. Bloom, Z. Yang, E. Lee, Extreme Fast Charge Challenges for Lithium-Ion Battery: Variability and Positive Electrode Issues, *J. Electrochem. Soc.* 166 (2019) A1926. <https://doi.org/10.1149/2.0731910jes>.
- [48] A.M. Kingston, A. Sakellariou, T. Varslot, G. Myers, A. Sheppard, Reliable automatic alignment of tomographic projection data by passive auto-focus, *Medical Physics* 38 (2011) 4934–4945. <https://doi.org/10.1118/1.3609096>.
- [49] P. Blažek, P. Westenberger, S. Erker, A. Brinek, T. Zikmund, D. Rettenwander, N. Peter, J. Keckes, J. Kaiser, T. Kazda, P. Vyrubal, M. Macak, J. Todt, Axially and radially inhomogeneous swelling in commercial 18650 Li-ion battery cells, *Journal of Energy Storage* 52 (2022) 104563. <https://doi.org/10.1016/j.est.2022.104563>.
- [50] P. Liu, W. Zhang, X. Liu, Y. Zhang, F. Wu, Electrochemical Impedance Analysis of C/LiFePO₄ Batteries in Cycling Process, *IOP Conf. Ser.: Mater. Sci. Eng.* 452 (2018) 032088. <https://doi.org/10.1088/1757-899X/452/3/032088>.
- [51] C. Busà, M. Belekoukia, M.J. Loveridge, The effects of ambient storage conditions on the structural and electrochemical properties of NMC-811 cathodes for Li-ion batteries, *Electrochimica Acta* 366 (2021) 137358. <https://doi.org/10.1016/j.electacta.2020.137358>.
- [52] H.-J. Noh, S. Yoon, C.S. Yoon, Y.-K. Sun, Comparison of the structural and electrochemical properties of layered Li[Ni_xCo_yMn_z]O₂ ($x = 1/3, 0.5, 0.6, 0.7, 0.8$ and 0.85) cathode material for lithium-ion batteries, *Journal of Power Sources* 233 (2013) 121–130. <https://doi.org/10.1016/j.jpowsour.2013.01.063>.